AD-A109 902 SCIENCE APPLICATIONS INC MCLEAN VA F/G 4/2
NEAR-INERTIAL MOTIONS: A PRELIMINARY MODEL-DATA COMPARISON.(U)
JAN 82 D RUBENSTEIN N00014-81-C-0084
UNCLASSIFIED SAI-82-620-WA NL

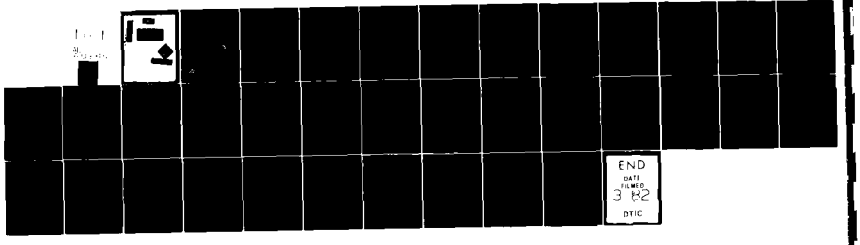

NEAR-INERTIAL MOTIONS: A PRELIMINARY MODEL-DATA COMPARISON

SAI-82-620-WA

SAI
ATLANTA • ANN ARBOR • BOSTON • CHICAGO • CLEVELAND • DENVER • HUNTSVILLE • LA JOLLA
LITTLE ROCK • LOS ANGELES • SAN FRANCISCO • SANTA BARBARA • TUCSON • WASHINGTON

NEAR-INERTIAL MOTIONS: A PRELIMINARY MODEL-DATA COMPARISON

SAI-82-620-WA

TR-OPD-81-274-10

January 1982

Prepared by:

David Rubenstein
Ocean Physics Division

Prepared for:

Naval Ocean Research and Development Activity
NSTL Station, Mississippi 39529

Final Report for Contract No. N00014-81-C-0084
and Technical Report for No. N00014-81-C-0075

SCIENCE APPLICATIONS, INC.
1710 Goodridge Drive
P.O. Box 1303
McLean, Virginia 22102
(703) 821-4300

UNCLASSIFIED

SECURITY CLASSIFICATION OF THIS PAGE (When Data Entered)

REPORT DOCUMENTATION PAGE	READ DISTRUCTIONS BEFORE COMPLETING FORM
1. REPORT NUMBER: SAI-82-620-WA 2. GOVT ACCESSION NO.: AD-A109 902	3. RECIPIENT'S CATALOG NUMBER
4. TITLE (and Subtitle): Near-Inertial Motions: A Preliminary Model-Data Comparison	5. TYPE OF REPORT & PERIOD COVERED: Technical Report May - October 1981 6. PERFORMING ORG. REPORT NUMBER: SAI-82-620-WA
7. AUTHOR(s): David Rubenstein	8. CONTRACT OR GRANT NUMBER(s): N00014-81-C-0075 N00014-81-C-0084
9. PERFORMING ORGANIZATION NAME AND ADDRESS: Science Applications, Inc. 1710 Goodridge Drive McLean, VA 22102	10. PROGRAM ELEMENT, PROJECT, TASK AREA & WORK UNIT NUMBERS
11. CONTROLLING OFFICE NAME AND ADDRESS: NORDA Code 540 Ocean Measurements Program NSTL Station, Bay St. Louis, MS 39529	12. REPORT DATE: January 1982 13. NUMBER OF PAGES
14. MONITORING AGENCY NAME & ADDRESS(if different from Controlling Office): Same	15. SECURITY CLASS. (of this report): UNCLASSIFIED 15a. DECLASSIFICATION/DOWNGRADING SCHEDULE

16. DISTRIBUTION STATEMENT (of this Report)

Approved for public release; distribution unlimited

17. DISTRIBUTION STATEMENT (of the abstract entered in Block 20, if different from Report)

Same

18. SUPPLEMENTARY NOTES

19. KEY WORDS (Continue on reverse side if necessary and identify by block number)

Inertial oscillations
Shear
Ocean Modeling

20. ABSTRACT (Continue on reverse side if necessary and identify by block number)

A summary of a wind-forced dynamical model of near-inertial motions is presented. Results from this model are briefly reviewed. Observations of coherence and response between wind stress and upper ocean currents are compared with model results.

DD FORM 1473 EDITION OF 1 NOV 65 IS OBSOLETE

UNCLASSIFIED

TABLE OF CONTENTS

LIST OF FIGURES

Section 1
INTRODUCTION

Pollard and Millard (1970) presented a mixed layer model of near-inertial frequency wind-induced current. This simple model is capable of simulating some of the important aspects of the response of inertial currents to wind stress. Kundu (1976) and Pollard (1980) also used this model, and showed comparisons with current meter data. The model has two parameters, a surface layer depth parameter and a linear decay rate parameter. By adjusting the parameter values, Kundu and Pollard optimized the agreement between the model and current meter data. Most of the inertial motions were shown to be linear responses to the wind-induced surface stress.

Krauss (1981) modeled the wind-induced response in the Baltic Sea, using a semispectral model. Krauss' model allows the specification of depth dependent profiles of eddy diffusivity and stratification. Krauss compared his model results with current meter data, and found that the erosion of the thermocline was due to the strong shear associated with inertial waves.

In many respects, the model we developed is quite similar to that of Krauss. In a previous report (Rubenstein, 1981b) we presented the mathematical details of our linear semispectral model. The equations are nearly the same as those from Krauss (1981), but the method of solution is much different. We solve the equations spectrally in the spatial dimensions and numerically in time. As a result

of this difference in solution methods, we are able to apply general, nonperiodic (in time) surface stress forcing functions. This capability is advantageous, as it allows us to emphasize the transient, time dependent nature of the inertial response.

In a previous report (Rubenstein and Newman, 1981) we presented statistical analyses of current meter data. These current meters were situated near Ocean Site D (39°10'N, 70°W), and collected data for about 48 days during the summer of 1970. Three moorings each held horizontal current meters at depths of 12, 32, 52, and 72 m, and also wind velocity recorders. Current and wind velocity were sampled at 15 minute intervals. The moorings were positioned roughly 50 km apart from each other. Additional details concerning the data set may be found in Pollard and Tarbell (1975) and in Pollard (1980).

In this technical note we report a preliminary assessment of our dynamical model. We do this by comparing results from our model with statistics from the current meter data. In particular, we compare the response spectra of current and shear to an imposed wind stress.

In Section 2 we summarize our dynamical model. We present the equations of motion and boundary conditions and briefly outline the method of solution. In Section 3 we discuss the methods used to compute the response functions. In Section 4 we compare the response functions from the model and the current meter data. We discuss these comparisons and speculate upon their implications.

Section 2
BRIEF MODEL DESCRIPTION

In this section we present the model equations and an outline of their method of solution. The interested reader is referred to Rubenstein (1981a) for a derivation of the equations, and to Rubenstein (1981b) for a complete description of their method of solution.

We consider a Boussinesq, hydrostatic ocean contained in a flat bottomed channel. The channel is of finite width and infinite length. The x-coordinate is aligned across the width, the z-coordinate is positive upwards. Table 2.1 is a list of the variables. The asterisks indicate that they are dimensional. The equations are listed below.

$$\frac{\partial u^*}{\partial t^*} - fv^* = -\frac{\partial p^*}{\partial x^*} + \frac{\partial}{\partial z^*}\left(\mu^* \frac{\partial u^*}{\partial z^*}\right) \tag{2.1}$$

$$\frac{\partial v^*}{\partial t^*} + fu^* = \frac{\partial}{\partial z^*}\left(\mu^* \frac{\partial v^*}{\partial z^*}\right) \tag{2.2}$$

$$0 = -\frac{\partial p^*}{\partial z^*} + b^* , \tag{2.3}$$

$$\frac{\partial b^*}{\partial t^*} + N^{*2} w^* = 0, \tag{2.4}$$

$$\frac{\partial u^*}{\partial x^*} + \frac{\partial w^*}{\partial z^*} = 0 \tag{2.5}$$

Table 2.1

DEFINITIONS OF VARIABLES

x^*, y^*, z^*	Right-handed coordinate system, z^* positive up, $z^* = 0$ at bottom, D at surface.
u^*, v^*, w^*	Velocity components
t^*	Time
p^*	p'/ρ_o, where p' is pressure fluctuation from a reference state, and ρ_o is a representative value of density
u^*	Eddy diffusivity, a function of z^* only
N^*	Vaisala frequency; $N^{*2} = -\left(\frac{g}{\rho_o}\frac{d\rho_r}{dz^*}\right)$, where $\rho_r(z^*)$ is a reference state of density.
b^*	Buoyancy; $-\rho' g/\rho_o$, where ρ' is density fluctuation from a reference state.

Here, we have set to zero all derivatives with respect to y^*. We have also neglected the buoyancy eddy diffusivity term and the processes which maintain the buoyancy profile against diffusion. The boundary conditions are as follows.

$$w^* = 0 \quad \text{at } z^* = 0, D, \tag{2.6}$$

$$\mu^* \frac{\partial u^*}{\partial z^*} = \mu^* \frac{\partial v^*}{\partial z^*} = 0 \text{ at } z^* = 0, \tag{2.7}$$

$$\mu^* \left(\frac{\partial u^*}{\partial z^*}, \frac{\partial v^*}{\partial z^*} \right) = -\underline{\tau}^* \left(x^*, t^* \right) \quad \text{at } z^* = D, \tag{2.8}$$

$$u^* = 0 \text{ at } x^* = 0, L. \tag{2.9}$$

The surface stress vector $\underline{\tau}^*(x^*,t^*)$ is a prescribed function which drives the system. Equations (2.6) and (2.9) state that velocities normal to the channel boundary surfaces should vanish. Equation (2.7) prescribes that the stress, and therefore the shear at the bottom should be zero. This boundary condition allows slippage at the bottom.

The equations are nondimensionalized and combined into two coupled equations in v and w. Approximate solutions are sought in the form of truncated Fourier-Chebyshev expansion;

$$v = \sum_{k=1}^{M} \sum_{j=0}^{N} V_{jk}(t) T_j(z) \sin k\pi x \tag{2.10}$$

$$w = \sum_{k=1}^{M} \sum_{j=0}^{N} W_{jk}(t) T_j(z) \cos k\pi x \, . \tag{2.11}$$

The functions $T_j(z)$ are j-order Chebyshev polynomials. The boundary conditions are satisfied by using the Tau method, discussed at great length by Gottlieb and Orszag (1977). With this method, the highest order behavior of the solution is determined not by the dynamical equations, but by the boundary conditions.

The resulting differential equations are first order in time for $V_{jk}(t)$, and second order for $W_{jk}(t)$. The second order equation is split into two first order equations. Starting initially from rest, these ordinary differential equations are then marched forward in time using a third order (three-step) Lax-Wendroff scheme. After numerically integrating the differential equations, (2.10) and (2.11) are expanded to give v and w as functions of x, z, and t. The continuity equation (2.5) is then used to obtain $u(x,z,t)$.

Section 3
RESPONSE FUNCTION COMPUTATIONS

3.1 GENERAL CONSIDERATIONS

We are interested in comparing the response functions predicted by the dynamical model with the response functions computed using the current meter data.

We let q represent some dynamical vector quantity, such as current or shear. We assume that $q(x,z,t)$ is a linear response to the wind stress, $\tau(x,t)$. The Fourier transforms of q and τ in horizontal wavenumber k and angular frequency ω space are written $Q(k,z,\omega)$ and $\Gamma(k,\omega)$, and are related by

$$Q(k,z,\omega) = H_q(k,z,\omega)\ \Gamma(k,\omega) \quad . \tag{3.1}$$

H_q is the complex-valued response function which relates q to the wind stress. This function may be decomposed into two parts;

$$H_q(k,z,\omega) = |H_q(k,z,\omega)|\ \exp\left[-i\phi_q(k,z,\omega)\right] \quad . \tag{3.2}$$

where the amplitude $|H_q(k,z,\omega)|$ is sometimes called the gain function, and $\phi_q(k,z,\omega)$ is the phase.

Following the notation in Bendat and Piersol (1971), we define the Fourier transforms in frequency over a finite duration T to be

$$Q(\omega) = \int_0^T q(t)e^{-i\omega t}\, dt, \tag{3.3}$$

$$\Gamma(\omega) = \int_0^T \tau(t)e^{-i\omega t}\, dt, \tag{3.4}$$

The one-sided power spectrum estimates are written

$$G_q(\omega) = \frac{2}{T} \left| Q(\omega) \right|^2, \tag{3.5}$$

$$G_\tau(\omega) = \frac{2}{T} \left| \Gamma(\omega) \right|^2. \tag{3.6}$$

The cross spectral estimate is written

$$G_{q\tau}(\omega) = \frac{2}{T} Q^*(\omega)\, \Gamma(\omega), \tag{3.7}$$

where the asterisk indicates a complex conjugate. Note that the auto spectra are real-valued, but the cross spectrum is complex-valued. The gain function and phase are given by

$$|H_q(\omega)| = \frac{|G_{q\tau}(\omega)|}{G_\tau(\omega)}, \tag{3.8}$$

$$\phi_q(\omega) = \tan^{-1}\left(\frac{\text{Im } G_{q\tau}(\omega)}{\text{Re } G_{q\tau}(\omega)}\right). \tag{3.9}$$

We can also write the coherence amplitude;

$$C(\omega) = \frac{|G_{q\tau}(\omega)|}{\sqrt{G_q(\omega)\, G_\tau(\omega)}}. \tag{3.10}$$

A few comments concerning the interpretation of coherence and response functions may be helpful to the reader. When these functions are computed, an implicit assumption is made, namely, that the system responds linearly to the input (driving) function. In the absence of contaminating noise, the response function is simply the ratio of the output Fourier transform to the input Fourier transform.

In the presence of contaminating noise, the response function is the ratio of the cross-spectral density function to the input spectral density function. Consider an ensemble of N estimates of the input and output Fourier transforms, $\Gamma_i(\omega)$ and $Q_i(\omega)$, i = 1,...,N. For any particular frequency bin $\omega \pm \Delta\omega$, we can plot sampled values of $Q_i(\omega)$ vs. $\Gamma_i(\omega)$. In analogy with regression analysis, the slope of the best-fit line through these sample points is given by the gain in (3.8). The coherence amplitude in (3.10) is a measure of the contaminating noise, and is directly analogous to a linear correlation coefficient.

3.2 MODEL RESPONSE

In order to elicit a model response to a wind stress, we drive the model with an impulse

$$\tau^y(x,t) = \hat{\delta}(t) \sin k\pi x \, (\rho_a/\rho_w) \quad , \tag{3.11}$$

where τ^y is the stress component in the y-direction. The ratio of air density to water density, ρ_a/ρ_w, allows us to convert the wind stress to surface stress, which directly drives the model.

The limiting case of a delta function--infinite amplitude and infinitesimal width--is not achievable using finite differences. Instead we apply a sharp impulse $\hat{\delta}(t)$ whose integral is unity;

$$\int_{-\infty}^{\infty} \hat{\delta}(\tau)\, dt = 1 \tag{3.12}$$

The Fourier transform of a delta function is unity. Therefore the response function is simply given by

$$H_q(k,\omega) = G_q(k,\omega). \tag{3.13}$$

3.3 RESPONSE COMPUTED FROM CURRENT METER RECORDS

The frequency response of a current or a shear time series to a wind stress is computed as follows. First, the wind stress vector is computed using the standard formulation

$$\underline{\tau} = C_d\, \underline{u}_o\, |\underline{u}_o|, \tag{3.14}$$

where $\underline{u}_o$ is the local wind vector, expressed in m/sec. The drag coefficient is computed following Amorocho and DeVries (1980);

$$C_d = 0.0015 \left[1 + \exp\left(\frac{|\underline{u}_o| - 12.5}{1.56}\right)\right]^{-1} + 0.00104. \tag{3.15}$$

Next, we follow the procedure described by Gonella (1972) for computing vector coherence functions. This procedure is outlined below.

1. Begin with two discrete vector time series, in complex form;

$$\underline{\tau}(t_n) = \tau^x(t_n) + i\tau^y(t_n)$$

$$\underline{u}(t_n) = u(t_n) + iv(t_n),$$

$$n = 0,1,\ldots, L-1 \qquad (3.16)$$

Here, $\underline{\tau} = (\tau^x, \tau^y)$ is the vector wind stress, and $\underline{u} = (u,v)$ is the current vector (or the difference between two vertically separated current records).

The integer L is chosen to be an integer M multiple of N, where N is a power of two:

$$L = MN \ . \qquad (3.17)$$

Divide each of the two time series into 2M-1 short series, overlapping one another by 50% and each of length N.

2. Multiply each of the short series by a Hanning window function.

3. The two-sided Fourier transform (the transform is not symmetric with respect to zero frequency) is computed for each short complex series;

$$\underline{T}(f_k) = \sum_{n=0}^{N-1} \underline{\tau}(t_n) \exp(-i2\pi kn/N)$$

$$\underline{U}(f_k) = \sum_{n=0}^{N-1} \underline{u}(t_n) \exp(-i2\pi kn/N)$$

$$k = -N/2,\ldots, N/2-1. \qquad (3.18)$$

4. The auto, coincident, and quadrature spectral density functions are computed:

$$P_1(f_k) = \langle \underline{\Gamma}(f_k)\, \underline{\Gamma}^*(f_k) \rangle$$

$$P_2(f_k) = \langle \underline{U}(f_k)\, \underline{U}^*(f_k) \rangle$$

$$P_{12}(f_k) - iQ_{12}(f_k) = \langle \underline{\Gamma}(f_k)\, \underline{U}^*(f_k) \rangle . \qquad (3.19)$$

The asterisks denote complex conjugates, and the brackets denote ensemble averages over the 2M-1 ensembles. This procedure provides estimates with 2M degrees of freedom.

5. Compute the coherence amplitude, phase, and gain (response amplitude), defined by

$$C(f_k) = \left[\frac{P_{12}^2 + Q_{12}^2}{P_{11} P_{22}} \right]^{1/2} , \qquad (3.20)$$

$$\phi(f_k) = \arctan\,(Q_{12}/P_{12}) , \qquad (3.21)$$

$$|H(f_k)| = \frac{\left[P_{12}^2 + Q_{12}^2 \right]^{1/2}}{P_{11}} \qquad (3.22)$$

for frequencies $f_k = k/(\Delta t N)$, for $k = -N/2 \ldots .N/2-1$. Negative frequencies indicate clockwise rotation and positive frequencies indicate counterclockwise rotation.

Section 4
PRELIMINARY MODEL-DATA COMPARISONS

4.1 GENERAL REMARKS

In this section we present the coherence and response functions of the current meter data, and compare the response amplitude functions with those predicted by the dynamical model. Prior to these presentations, it is appropriate to make several comments concerning the validity of the descriptive comparisons in Section 4.2 and the quantitative comparisons in Section 4.3.

Figure 4.1 shows profiles of Vaisala frequency in the upper 100 m, which were reported by Pollard (1980). These profiles show a strongly stratified thermocline centered at about 20 m, and weaker stratification below about 40 m.

Figure 4.2 shows the smoothed profiles of Vaisala frequency and eddy diffusivity that were used in the model simulations. The Vaisala frequency profile is similar to the profile observed at mooring 338 on July 23/24 1970, shown in Figure 4.1. Below 90 m the profile has been tapered to zero. The eddy diffusivity profile is patterned after the one used by Krauss (1981).

The spatial distribution of the wind stress field is an important aspect of our model-data comparisons. Pollard (1980) analyzed the length scales associated with the atmospheric front which passed Ocean Site D on

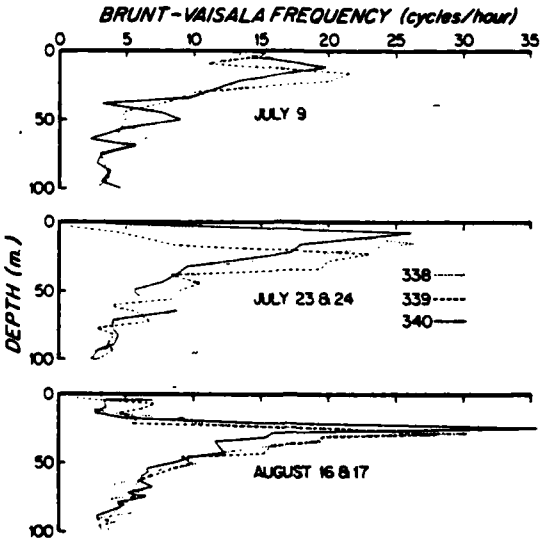

Figure 4.1 Vaisala frequency at the three moorings on 9 and 23/24 July and 16/17 August as functions of depth in the top 100 m. The profiles were computed using averaged values of density at approximately 5 m intervals, so details of the structure particularly in the top 15 m have been smoothed. From Pollard (1980).

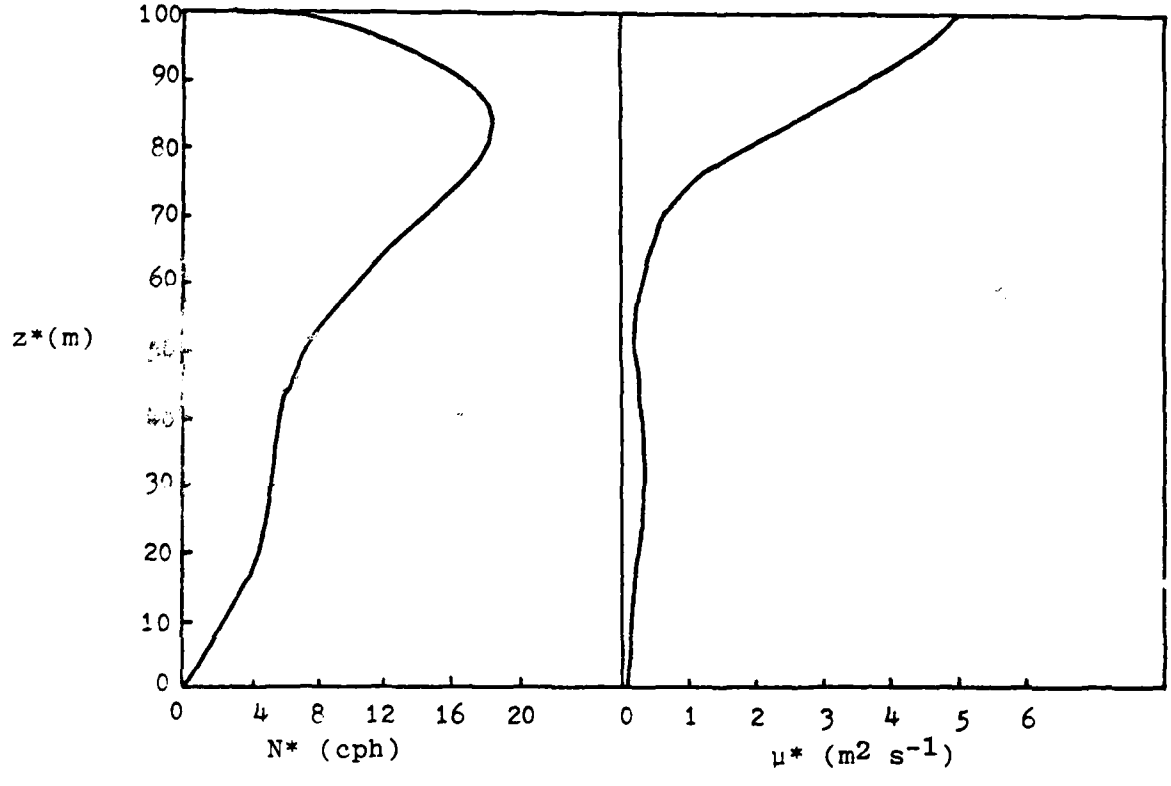

Figure 4.2 Profiles of Vaisala frequency (left) and eddy diffusivity (right) used in numerical model runs.

August 11, 1970. The length scale along the direction of propagation of the front is about 400 km, and the length scale perpendicular to the propagation direction is about 40 km.

Unfortunately, not much more is known about the spatial distribution of the wind stress field. The dynamical model solves the horizontal spatial structure in terms of Fourier modes. A quantitative comparison between the model and observations requires knowledge of the wind stress spatial distribution. In the absence of such knowledge, we will have to make an assumption in Section 4.3 concerning the spatial power spectrum of wind stress. We will assume that statistically, the predominant wind stress contribution has an associated wavelength greater than 300 km.

4.2 DESCRIPTIVE COMPARISON

Figure 4.3 shows the numerically computed response amplitude of shear (from equations (3.5) and (3.13)). The associated environmental profiles are shown in Figure 4.2. The contour labels represent the relative amplitude levels, at a depth of 25 m below the surface. The response amplitude is greatly emphasized in a narrow band (between the contours labeled 500) which coincides with the first vertical mode dispersion relation. In Rubenstein (1981b), there was evidence in the constant-stratification case of second and third modes. Here too, there is also a slight hint of an outline of the second vertical mode (in the region bounded by the contour labeled 100, near $\omega/f = 1.2$, $k^* = 0.3$ km^{-1}).

Figure 4.4 shows a numerically computed response phase function. This example is for the response of the

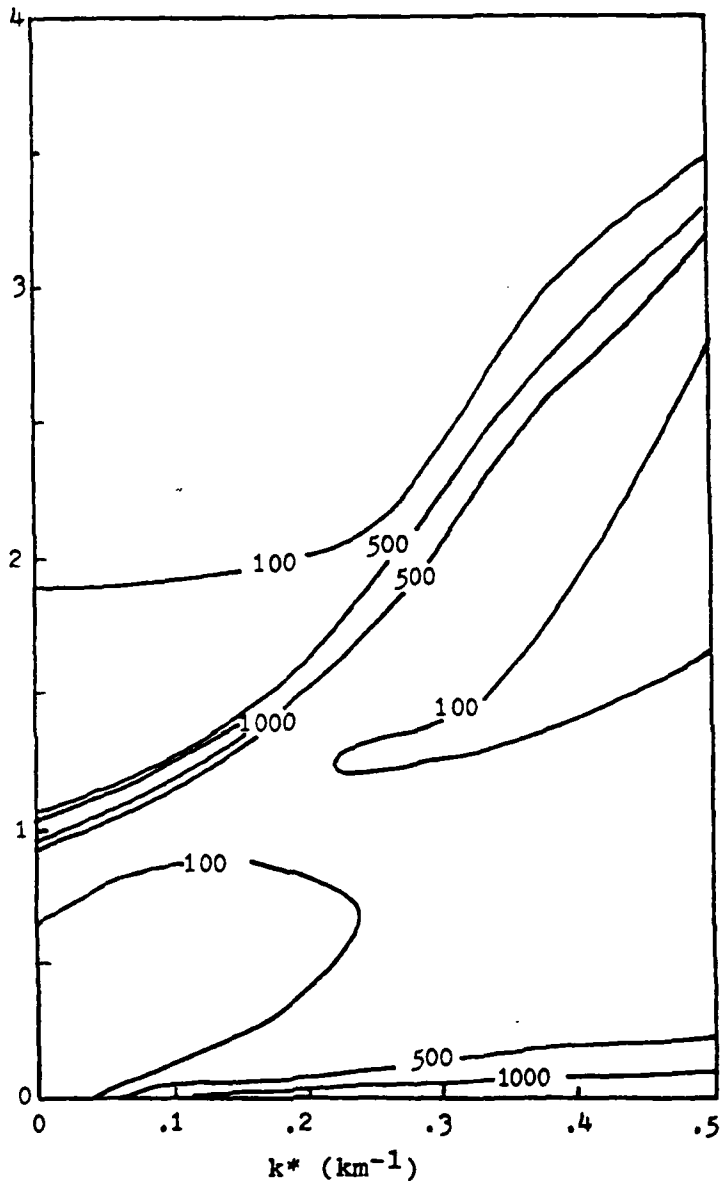

Figure 4.3 Relative amplitude response of shear, for the nonuniform stratification and eddy diffusivity profiles shown in Figure 4.2. The channel depth is 100 m. This figure shows the response at a depth of 25 m below the surface ($z^*/D = 0.75$).

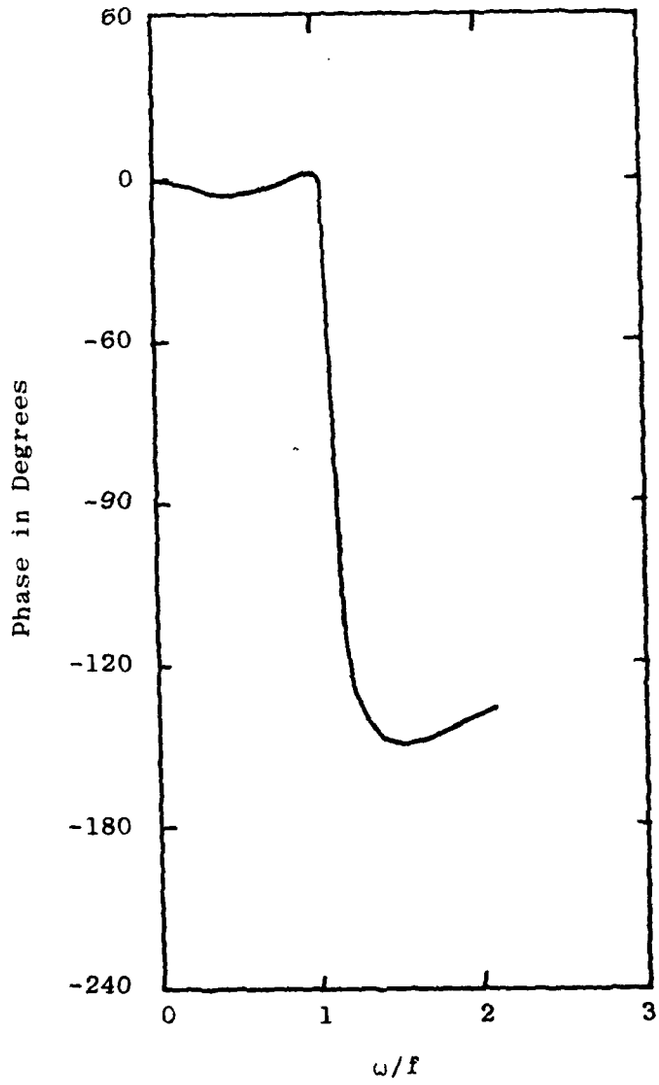

Figure 4.4 Numerically computed response phase function for v-component of current, at 12 m depth, for horizontal wavenumber $k^* = 0$.

v-component of current, for horizontal wavenumber $k^* = 0$. The phase is nearly constant below the inertial frequency, f. At the inertial frequency, the phase shifts sharply by about 160 degrees. This behavior is characteristic of resonant types of responses.

Rubenstein (1981b) developed an analytic solution to the initial start-up problem. The inviscid internal waves equation was solved, subject to various formulations of time dependent Ekman pumping boundary conditions. In a uniformly stratified fluid, the resonant response amplitude of vertical velocity to an impulsive driving force is proportional to

$$w_j \propto \frac{\omega_j^2 - f^2}{j\omega_j} \tag{4.1}$$

where ω_j is the j'th eigenfrequency, and the index j is the vertical mode number. As w_j is inversely proportional to j, the first mode j = 1 should be predominant. This result is in agreement with Figure 4.3.

Using these insights, we can descriptively evaluate the response functions of selectively chosen current meter records. Figure 4.5 shows the coherence amplitude, phase, and gain functions computed between the wind stress measured by wind recorder #3391 and the current measured by the current meter #3393, at 12 m depth. We remind the reader that negative frequencies indicate clockwise vector rotation, and positive frequencies indicate counterclockwise rotation. The most noticeable feature is the strong peak in the gain function at the inertial frequency, 0.0527 cph. The coherence amplitude at the

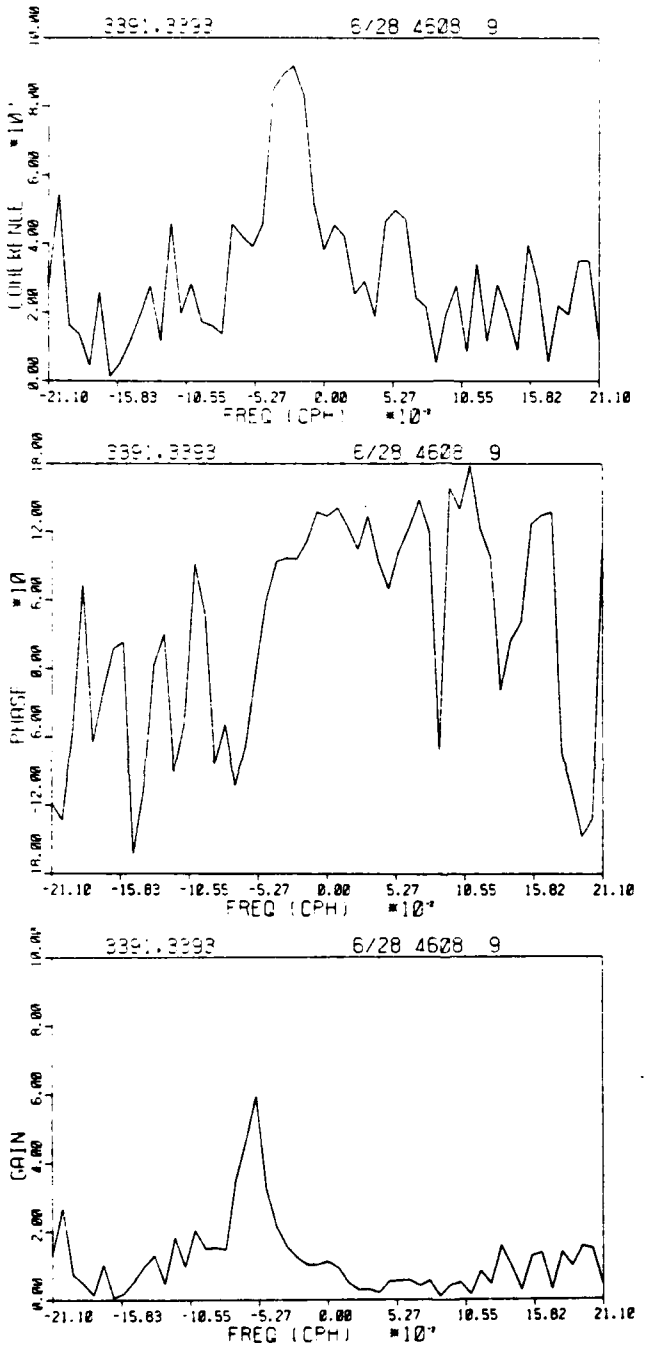

Figure 4.5 Coherence amplitude, phase, and gain (response amplitude) functions computed between wind stress (#3391) and 12 m current (#3393). Gain is in units (m/sec)-1.

inertial frequency is about 0.4, whereas the 80% confidence level is 0.48. The implication is that noise at the inertial frequency (for example, inertial oscillations due to non-local forcing) may be contaminating the system response. We also note that the phase shifts by about 180 degrees, in the vicinity of the inertial frequency.

Now consider Figure 4.6, which displays the coherence and response functions computed between the wind stress (#3401) and 12 m depth current (#3402). The coherence is high in the frequency range $0 \gtrsim \omega \gtrsim -.06$ cph. The gain function is dominated by three peaks. The strongest peak is centered at the inertial frequency. Since the coherence amplitude is high at this frequency, this peak represents oscillations which are responding to the local wind stress.

The second biggest peak is at 0.085 cph, and is due to tides at the semidiurnal frequency. The fact that the coherence at this frequency is low also helps to reinforce our belief that this peak is not a response to the local wind forcing.

The third peak is situated at a frequency of 0.132 cph. There is also a coherence peak coincident with this frequency. This coherence peak may possibly be a fortuitous result of the way in which currents and wind-stress were measured. Currents measured in the vicinity of a sharp density interface (as in the present case) depend nonlinearly on small vertical displacements of the interface. The deviation of our parameterization of wind stress in (3.14) and (3.15) from the true wind stress depends nonlinearly on the wind speed. Also, nonlinear

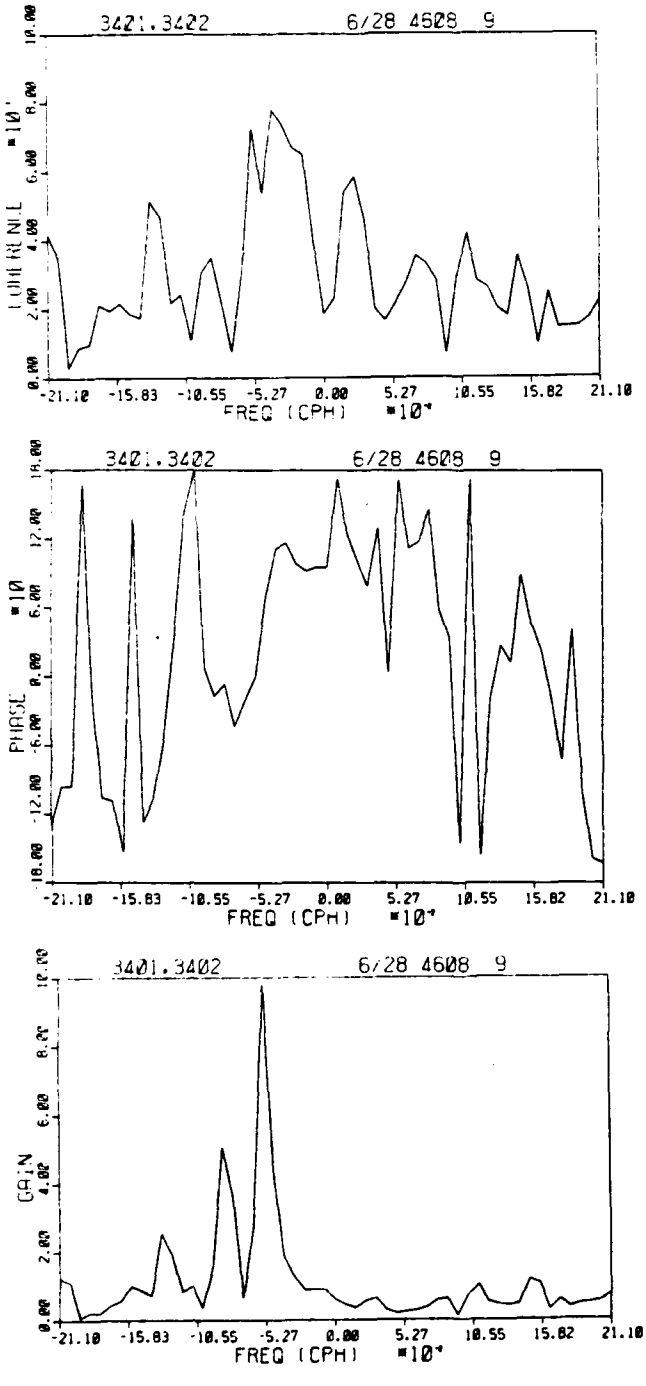

Figure 4.6 Coherence amplitude, phase, and gain (response amplitude) functions computed between wind stress (#3401) and 12 m current (#3402). Gain is in units (m/sec)-1.

wind-induced motions of the surface buoy may be transmitted through the mooring cable to the current meters. A combination of these unrelated nonlinear effects--in the wind stress and in the measured response--may result in an artificial coherence peak, whose frequency is the sum of the inertial and semidiurnal frequencies.

The vertical shear, computed by taking the difference between pairs of vertically adjacent current records, shows similar characteristics. As an example, Figure 4.7 shows the coherence and response functions between the wind stress (#3391) and the current meter pair (#3393, 3394) located at 12 m and 32 m depth. Most striking are the two peaks in the gain function, one at the inertial frequency and the second at twice the inertial frequency. Both peaks are associated with high coherence amplitude. In analogy with the third spectral peak in Figure 4.6, the peak in Figure 4.7 is possibly a fortuitous result of the way in which currents and wind stress were measured.

The situation is further complicated by the evidence for nonlinear interactions in power spectra of currents and shears, discussed by Rubenstein and Newman (1981). A number of these spectra show small peaks at the frequency 0.132 cph, the sum of the inertial and semidiurnal frequencies. This nonlinear interaction may feed energy into the internal wave field, and may result in radiation damping of the inertial oscillations in the mixed layer. Unfortunately, our dynamical model is linear and is unable to simulate such a process.

4.3 QUANTITATIVE COMPARISON

In this section we present quantitative comparisons between the response amplitude (gain) functions

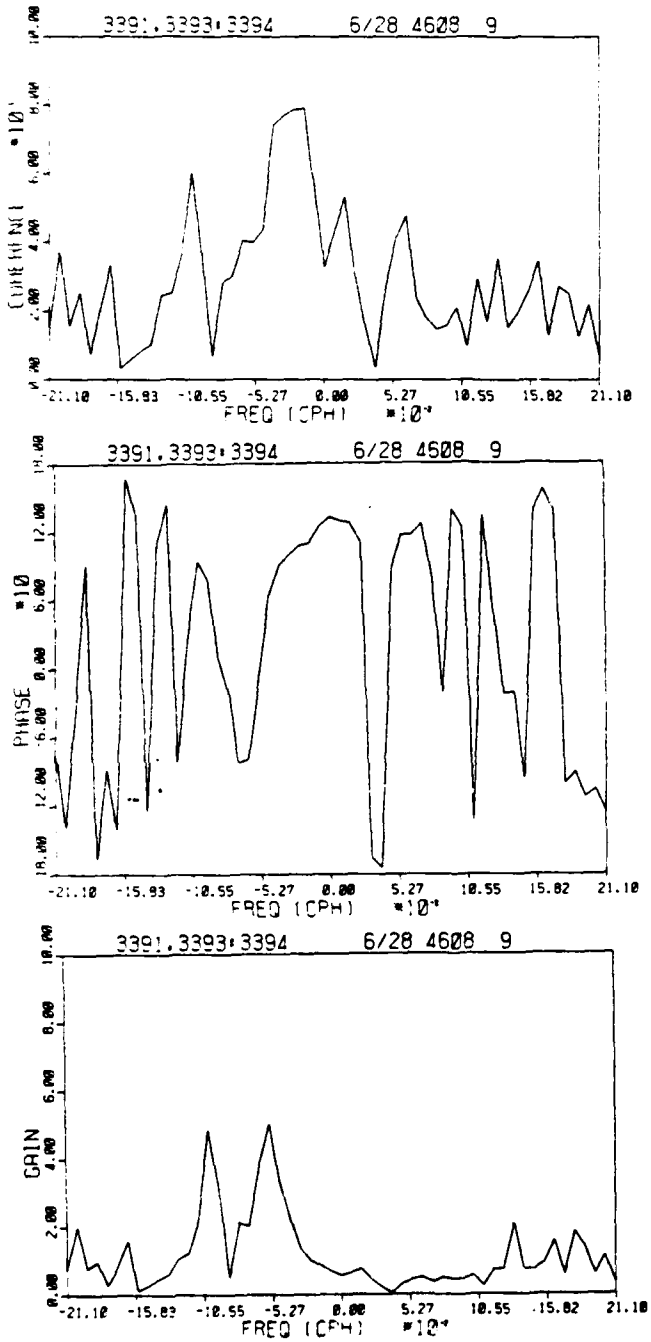

Figure 4.7 Coherence amplitude, phase, and gain (response amplitude) functions computed between wind stress (#3391) and current meter velocity difference (#3393-#3394). Gain is in units (m/sec)-1.

predicted by the numerical model for horizontal current and shear, and the average response amplitudes computed from current meter observations. The purpose is not to show exact agreement between theory and observations. Instead, we show that the numerical solutions are of the correct order of magnitude. Further fine tuning of the model should be able to improve the agreement.

Figure 4.8 shows a comparison between the observed and simulated gain functions. The solid curve represents the average gain function for the three pairs of wind recorders and uppermost current meters. This curve is a mirror image about zero frequency, and represents the clockwise rotary spectrum. The dashed curve labeled "A" represents the simulated gain function between wind stress and the current speed. The eddy diffusivity profile used for this simulation is shown in Figure 4.2, and there is no stratification. From the point of view of the model equations, the statement that there is no stratification is equivalent to the assertion that the wind stress does not vary in space. In effect, we are assuming that the length scale over which the wind stress varies is greater than 300 km. This assumption is supported by Pollard's (1980) estimate that the horizontal wavelength of inertial oscillations lies in the range 700-1700 km.

We see that the modeled response is too sharp; the magnitude agrees at the inertial frequency, but in the remainder of the frequency domain the model underestimates the observed response function. By increasing the eddy diffusivity profile by a factor of two (Case B), the

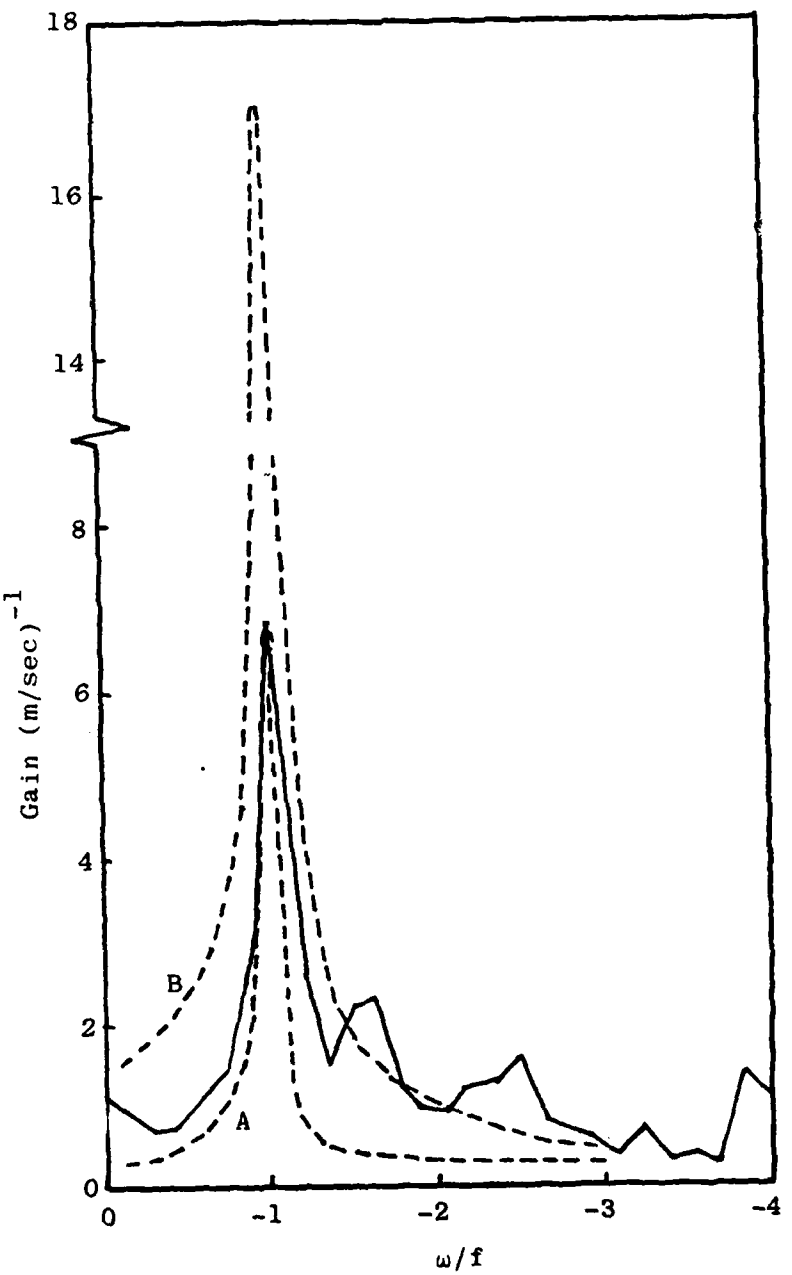

Figure 4.8 Comparison between observed (solid line) and simulated (dashed lines) gain functions. Gain is computed between wind stress and current at 12 m depth. Eddy diffusivity profile used for Case A is shown in Figure 4.2, and Case B uses the same profile, multiplied by a factor of two.

modeled response increases, but the sharpness of the resonance remains the same.

Figure 4.9 compares the observed response of velocity difference to the modeled response of shear. The comparison is very similar to the current response in Figure 4.8, and the same remarks apply here.

4.4 CONCLUSIONS AND FUTURE WORK

Krauss (1976) showed that the shape of internal wave resonances changes as the shape of the eddy diffusivity profile is varied. The ratio of eddy diffusivity in the surface layer to that in the interior is the most important aspect of the profile shape. By varying this ratio, it should be possible to fine tune our model, and to obtain better agreement with the observed response. Our purpose here is not to perform this fine tuning, but instead to show that there is good general agreement between model and observations. In SAI's Fiscal Year 1982 effort for NORDA's Ocean Measurement Program, we plan to examine the sensitivity of the model to variations in the eddy diffusivity and Vaisala frequency profiles. After optimizing the comparison of the response functions in the frequency domain, we plan to extend the comparison into the time domain.

The observations of response amplitude of current and shear show peaks at the inertial frequency, and in some cases at the semidiurnal tidal frequency and at somewhat higher frequencies as well. The semidiurnal tidal peaks

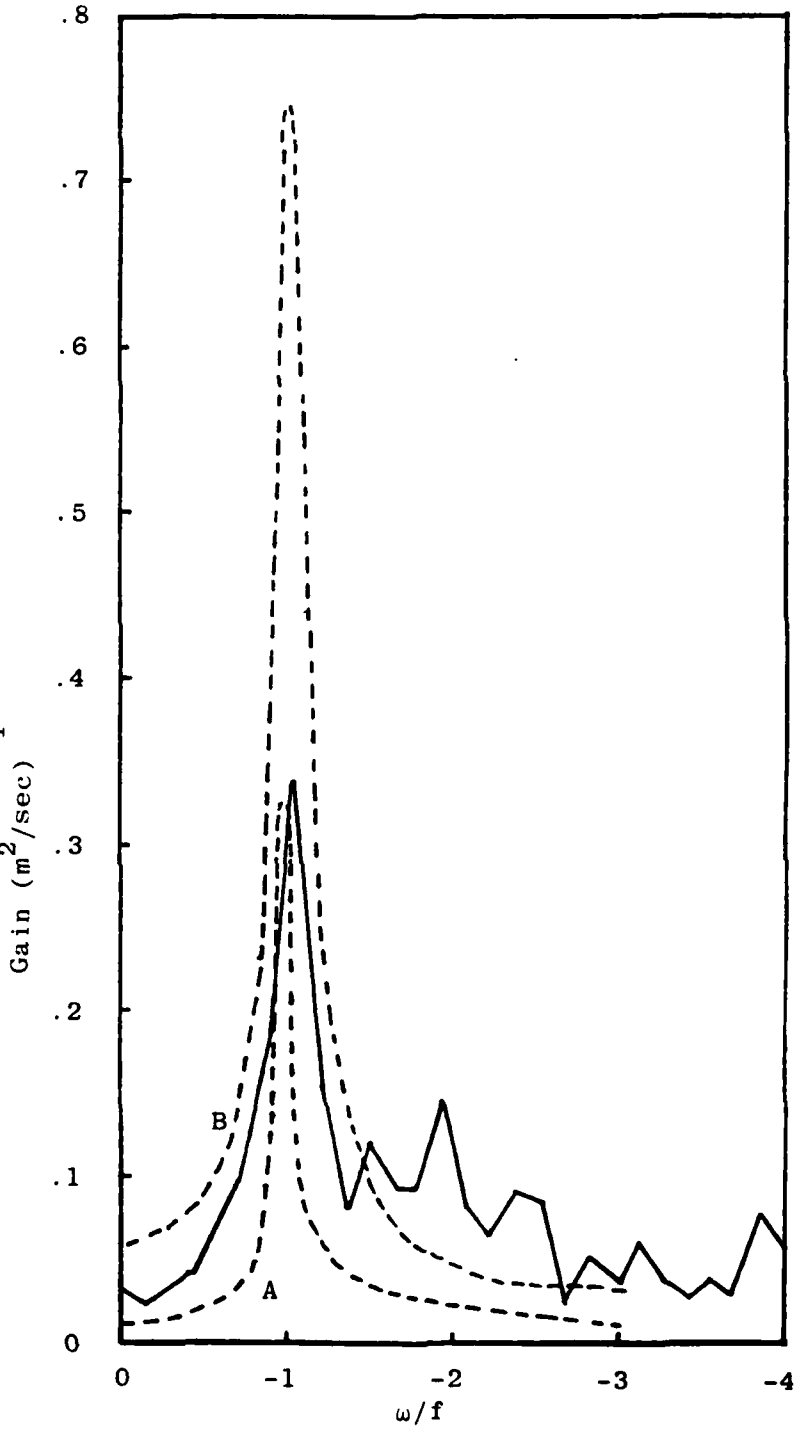

Figure 4.9 As in Figure 4.8, but for simulated shear at 25 m (dashed lines) and shear between 12 m and 32 m current meters (solid line).

cannot be predicted by our model of wind-induced shear. We do not expect these peaks to be as significant in the open ocean, far from regions of strong bottom topography.

We hypothesize that some fraction of the response in the internal wave band (with frequency greater than the inertial frequency) is due to transient atmospheric events, such as fronts, whose horizontal length scales are small. It may be possible to test this hypothesis through further analysis of this set of current meter data, and other data sets. Such a test would entail comparisons of the response functions computed during periods of intense wind forcing events, with others during calm atmospheric conditions. If these wind events have the shorter wavelength components which are requisite for the excitation of internal waves, then they will be associated with greater spectral response in the internal wave band.

It may also be possible to test this hypothesis using our dynamical model. This could be done by applying a wind stress whose spatial dependence is more realistic than the simplistic sinusoidal dependence in equation (3.11). Wind stress patterns, whose spatial characteristics are similar to fronts, could be applied to the model. The response functions thus obtained should be more realistic in the internal wave band than those plotted in Figures 4.8 and 4.9.

REFERENCES

Amorocho, J. and J.J. DeVries, 1980: A New Evaluation of the Wind Stress Coefficient Over Water Surfaces. J. Geophys. Res., 85, 433-442.

Bendat, J.S., and A.G. Piersol, 1971: Random Data: Analysis and Measurement Procedures, John Wiley and Sons, Inc., New York.

Gonella, J., 1972: A Rotary-Component Method for Analyzing Meteorological and Oceanographic Vector Time Series. Deep Sea Res., 19, 833-846.

Gottlieb, D. and S.A. Orszag, 1977: Numerical Analysis of Spectral Methods, Cambridge Hydrodynamics, Inc., pp. 273.

Krauss, W., 1981: The Erosion of a Thermocline, J. Phys. Oceanogr., 11, 415-433.

Pollard, R.T., and R.C. Millard, 1970: Comparison Between Observed and Simulated Wind-Generated Inertial Oscillations. Deep-Sea Res., 17, 813-821.

Pollard, R.T., 1980: Properties of Near-Surface Inertial Oscillations, J. Phys. Oceanogr., 10, 385-398.

Pollard, R.T., and S. Tarbell, 1975: A compilation of Moored Current Meter and Wind Observations, Volume VIII (1970 Array Experiment), Woods Hole Oceanographic Institution, Ref. 75-7.

Rubenstein, D.M., 1981a: Models of Near Inertial Vertical Shear. Science Applications, Inc., Ocean Physics Div., McLean, VA. SAI-82-564-WA.

Rubenstein, D.M., 1981b: A Dynamical Model of Wind-Induced Near-Inertial Motions. Science Applications, Inc., Ocean Physics Div., McLean, VA. SAI-82-598-WA.

Rubenstein, D.M., and F.C. Newman, 1981: Analysis and Interpretation of Shear from Ocean Current Meters. Science Applications, Inc., Ocean Physics Div., McLean, VA. To be submitted.

END

DATE
FILMED
3-82

DTIC